

Vortex dynamics and transport phenomena in stenotic aortic models using Echo-PIV

Javier Brum¹, Miguel Bernal^{2‡}, Nicasio Barrere³, Carlos Negreira¹ and Cecilia Cabeza³

¹ Laboratorio de Acústica Ultrasonora, Instituto de Física, Facultad de Ciencias, Universidad de la República, Iguá 4225, 11400, Montevideo, Uruguay

² Grupo de Dinámica Cardiovascular, Universidad Pontificia Bolivariana, Medellín, Colombia

³ Física No Lineal, Instituto de Física, Facultad de Ciencias, Universidad de la República, Iguá 4225, 11400, Montevideo, Uruguay

E-mail: jbrum@fisica.edu.uy

Abstract.

Atherosclerosis is the most fatal cardiovascular disease. As disease progresses, stenoses grow inside the arteries blocking their lumen and altering blood flow. Analysing flow dynamics can provide a deeper insight on the stenosis evolution. In this work, we propose a novel approach which combines ultrasound with Eulerian and Lagrangian descriptors, to analyse blood flow dynamics and fluid transport in stenotic aortic models with morphology, mechanical and optical properties close to those of real arteries. To this end, vorticity, particle residence time (PRT), particle's final position (FP) and finite time Lyapunov's exponents (FTLE) were computed from the experimental fluid velocity fields acquired using ultrasonic particle imaging velocimetry (Echo-PIV). For the experiments, CT-images were used to create morphological realistic models of the descending aorta with 0%, 35% and 50% occlusion degree with same mechanical properties as real arteries. Each model was connected to a circuit with a pulsatile programmable pump which mimics physiological flow and pressure conditions. The pulsatile frequency was set to ≈ 0.9 Hz (55 bpm) and the upstream peak Reynolds number (Re) was changed from 1100 to 2000. Flow in the post-stenotic region was composed of two main structures: a high velocity jet over the stenosis throat and a recirculation region behind the stenosis where vortex form and shed. We characterized vortex kinematics showing that vortex propagation velocity increases with Re . Moreover, from the FTLE field we identified Lagrangian Coherent Structures (i.e. material barriers) that dictate transport behind the stenosis. The size and strength of those barriers increased with Re and the occlusion degree. Finally, from the PRT and FP, we showed that independently of Re , the same amount of fluid remains on the stenosis over more than a pulsatile period, which combined with large FTLE values may provide an alternative way to understand stenosis growth.

Keywords: lagrangian coherent structures, ultrasound, blood flow dynamics, atherosclerosis

‡ Present address: Verasonics Inc, 11335 NE 122nd Way, Suite 100, Kirkland, WA 98034, USA

Vortex dynamics and transport phenomena in stenotic aortic models using Echo-PIV 2

Submitted to: *Phys. Med. Biol.*

1. Introduction

Cardiovascular diseases represent one of the major causes of death in the world [1]. Blood flow dynamics has shown to be crucial in understanding the different causes of gradual or acute changes during diseases affecting the cardiovascular system. For example, flow pattern and vortex dynamics in the left ventricle are correlated with altered cardiac function [2, 3, 4]. In arteries, regions of disrupted flow or with large recirculation are likely to favor atherosclerosis [5, 6], one of the most prevalent and dangerous cardiovascular disease [1]. In atherosclerosis fat, cholesterol and other substances accumulate inside the artery creating a plaque or stenosis which narrows the arterial lumen. During growth or plaque rupture, atherosclerosis may lead to heart failure, stroke or even death. However, despite its danger, the mechanisms of stenosis evolution and rupture remain poorly understood.

Eulerian approaches have shown to be a powerful tool in analysing blood flow dynamics in stenotic vessels [7, 8, 9, 10, 11, 12]. In these works, streamlines, vorticity, turbulent kinetic energy and wall shear stresses were computed from the instantaneous velocity data obtained either via numerical studies [7, 8], in vitro experiments [9, 10, 11] or both [12]. Alternatively, Lagrangian descriptors can provide direct information on the transport topology in large vessels (e.g. flow mixing, stirring, recirculation, stagnation and separation) [13]. Analysing the transport topology in stenotic vessels may provide valuable information on how stenosis grows and eventually ruptures [14, 15, 16].

Lagrangian Coherent Structures (LCS) are the most common Lagrangian descriptors and are usually defined as locally strongest attracting or repelling material barrier [17, 18]. They reveal structures that govern fluid transport and mixing in complex flows and have been applied to oceanography, geophysics and atmospheric flows (please refer to references within the reviews [17, 18]). Another Lagrangian descriptor is the fluid Particle Residence Time (PRT), which measures the time that a fluid parcel spends in a given region. Recently LCS and PRT have been applied to study hemodynamics in the left ventricle [19, 20, 21, 22, 23, 24, 25] and large vessels [26, 27, 28, 29, 16, 30, 13, 31].

However, despite the numerous works involving hemodynamics in pathological conditions, only a few have focused on studying flow dynamics in stenotic vessels. In the experimental work of Jerónimo *et al.* [28, 29] PRT was measured using two dimensional particle tracking velocimetry in steady and unsteady flow conditions for different Reynolds and Strouhal numbers. As vessel model, they used a rigid acrylic pipe with a smooth axisymmetric constriction followed by an unrealistic sudden expansion. Other works used instantaneous velocity data obtained either via numerical studies [7, 8, 12] or in vitro experiments [9, 10, 11, 12]. Numerical studies can account for patient specific morphology [8], providing highly resolved three-dimensional velocity fields. However, they are unable to simulate the mechanical properties of the vessel wall, which is always assumed to be rigid. This is also the case for the experiments [9, 10, 11, 12] where transparent models made of acrylic or silicone are required because

optical particle velocimetry is used to measure the fluid velocity field. For example, in the work of Usmani *et al.* [12] they used a compliant stenotic model made of silicone where its distensibility was changed by modifying the wall thickness of the model. This type of material does not mimic the anisotropic, non-linear, elastic behaviour of the vessel wall. Finally, these works focus on studying flow from an Eulerian perspective. To our knowledge, no experimental work reported the use of LCS to study flow in stenotic vessels.

Consequently, in this work we present a novel approach to study vortex dynamics and fluid transport in stenotic aortic models with morphology, mechanical and optical properties close to those of real arteries. To this end, vorticity, LCS, PRT and final position (FP) maps were computed from the particle velocity fields acquired using ultrasonic particle imaging velocimetry (Echo-PIV). The flow dynamics behind the stenosis was studied as a function of Reynolds number and the degree of occlusion. Finally, results were discussed and compared to those reported in the literature.

2. Materials and Methods

2.1. Model Manufacturing

The aortic models for this study were developed following the same procedure described in Bernal *et al.* [32]. By segmentation of anonymous CT-images of a healthy patient, the lumen and the adventitia layer of the descending aorta were reconstructed (lumen volume and inflated volume in Fig. 1(a)). For each geometry (lumen and inflated), two molds were fabricated using computer numerically controlled machine. Then, the lumen volume was inserted into the mold created from the inflated geometry (Fig. 1(b)). The gap between these two elements allowed the injection of a 10% b/w Polyvinyl Alcohol (PVA) solution. Prior to the injection of the polymer, the core was wrapped with a reinforcing fabric to allow the models to withstand physiological pressure levels and to have mechanical properties similar to that of healthy arteries [33, 32]. Finally, the whole setting was subject to 7 cycles of freezing and thawing to polymerize PVA, after which the mold was opened and the core was removed. The models dimensions were 17 cm in length, 2.4 cm of external diameter and ≈ 0.3 cm of wall thickness. For healthy physiological pressures (diastolic/systolic) of 80/120 mmHg, the models exhibit a nonlinear change in their shear modulus from ≈ 133 kPa to ≈ 209 kPa with 10% of error. These values are very similar to those of swine aortas [33, 32]. Precise details on the mechanical evaluation of the models are given in the works of Bernal *et al.* [33, 32].

Additional models with different degree of occlusion were made by modifying the lumen geometry resulting in a stenosis made of PVA (Fig. 1(b)). The profile of the stenosis was chosen to be Gaussian following $z_{st} = A_o \exp[-x/(2\sigma^2)]$ where z_{st} is the height of the stenosis and $\sigma = 1.85$ cm, which gives a full width at half maximum of ≈ 4.35 cm. The value of A_o was chosen to achieve an occlusion maximum height of ≈ 0.8 cm and ≈ 1.2 cm which resulted in two different models with 35% and 50% of

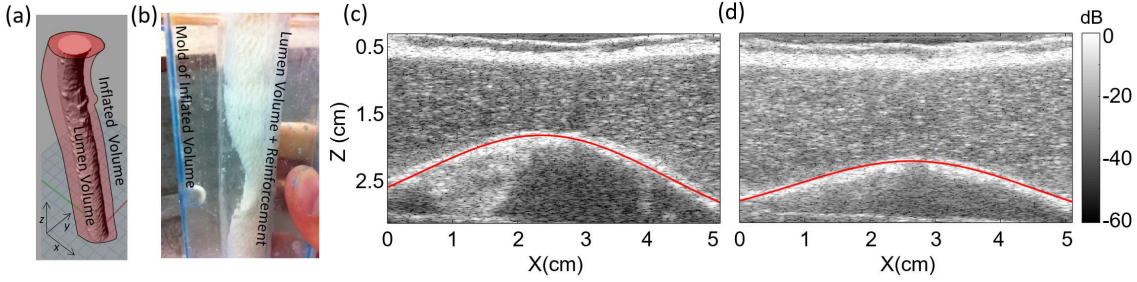


Figure 1. Manufacturing process of the stenotic aortic models. **(a)** Reconstructed volumes from CT-images: lumen volume in grey and inflated volume in red shadow. **(b)** Lumen volume wrapped in the reinforcing fabric inside the acrylic mold created from the inflated volume. Cross-sectional B-mode images of the models presenting a **(c)** 50% and **(d)** 35% occlusion in diameter. The red full line corresponds to the Gaussian profile used to create the stenosis.

occlusion in diameter, respectively. The shear modulus of the stenosis was 30 kPa and was evaluated by shear wave elastography. Figures 1(c) and 1(d) show a cross sectional B-mode image of each of the stenotic models with the Gaussian profile highlighted by a full red line.

2.2. Hemodynamic simulator

Each model was connected to a hemodynamic work bench simulator, which has already been used for the elasticity assessment under physiological conditions of vascular grafts, vessel models and femoral ovine arteries [34, 32]. The simulator consists of a programmable piston pump that mimics flow and pressure wave from the heart [35], two pressure sensors (one at the inlet of the model and one at the outlet), a reservoir that could be pressurized using a manual sphygmomanometer and a water bath where the model is placed.

2.3. Echo-PIV

The fluid velocity field was measured through ultrasonic particle imaging velocimetry (Echo-PIV), which is based on 2D cross-correlation of consecutive speckle images [36, 37, 38]. To this end, the circuit was filled with degassed water seeded with neutrally buoyant polyamide particles (Dantec Dynamics, Denmark) with a mean diameter of 50 μm . These particles have a Stokes number of approximately 1×10^{-4} and can be assumed to closely follow the flow. A particles density of 0.2 gr/L was used in all the experiments.

For Echo-PIV, ultrasonic B-mode images were acquired using plane wave insonification [39] at 200 Hz frame rate during 2.5 s. A custom-made linear probe (Vermon, Tours, France) with 256 elements (0.2 mm pitch) working at 15 MHz driven by a Verasonics Research Ultrasound System was used in the experiments. The axial resolution (i.e. along depth) of the B-modes images was 0.1 mm. The cross sectional centre plane of the model was imaged by positioning the probe parallel to the aortic

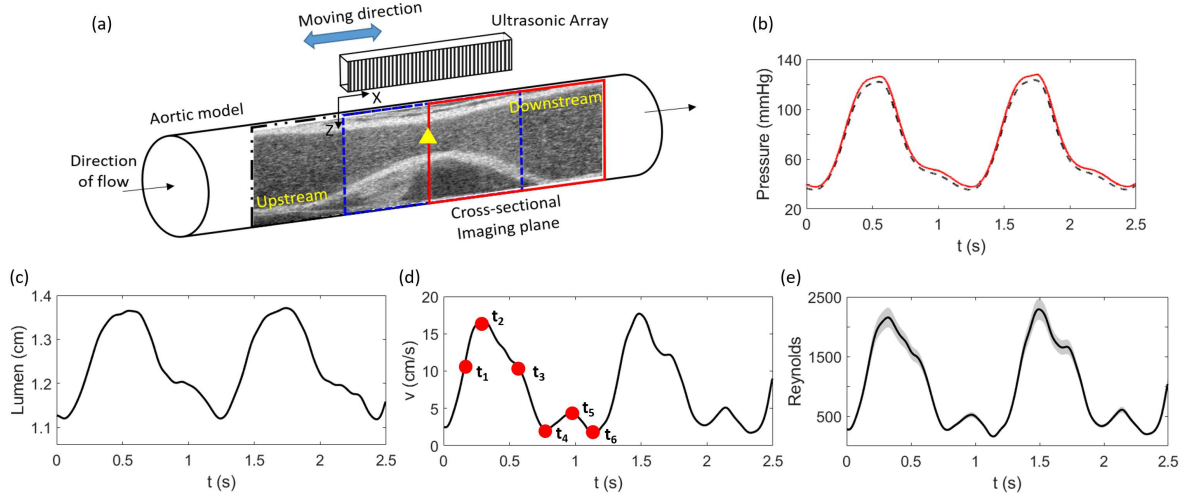


Figure 2. Echo-PIV setup and flow conditions. **(a)** Sketch of the ultrasonic probe positioning and movement along the cross-sectional centre plane of the aortic model (xz -plane). The three ROIs upstream, on the stenosis and post-stenotic are indicated by a black dotted-dashed, blue dashed and solid red rectangles, respectively. **(b)** Pressure at the inlet (red solid line) and outlet (black dashed line) of the 50% occluded model for $Re = 2000$ experiment. **(c)** Lumen size and **(d)** velocity as a function of time measured at the centreline of the stenosis throat indicated by a yellow triangle on panel (a). **(e)** Re number computed from panels (c) and (d). The gray shadow indicates the error on Re due to the error on the diameter which is ≈ 0.1 cm.

model with its first element facing towards the direction of the flow (Fig. 2(a)). To avoid constraint the movement of the wall, the ultrasound probe was not in direct contact with the model using the water bath as coupling medium between probe and model. As illustrated in Fig. 2(a) by different coloured rectangles, three Regions of Interest (ROI) were imaged in the experiments: upstream (black dashed-dotted line), post-stenotic (red full line) and on the stenosis throat (blue dashed line). To image these three ROIs the probe was moved along the x -direction by a step by step motor. For each experiment, a time lapse of ten periods was waited before the ultrasound acquisition to avoid start-up effects.

Finally, PIVlab software was used to compute the velocity fields from the B-mode images using a direct correlation approach with windows of $0.64 \times 0.32 \text{ cm}^2$ and 75% overlap [40]. This resulted in a lateral and axial resolution for the velocity fields of 1.6 mm and 0.8 mm, respectively.

2.4. Flow Conditions

The pulsatile frequency was set to ≈ 0.9 Hz (55 bpm) for all the experiments, close to that of a normal human heart. Moreover, the pressure wave form was set to be close to the physiological pressure wave for the descending aorta [41]. Figure 2(b) shows representative pressures at the inlet and outlet of the 50% occluded model.

Given a fixed flow rate, flow dynamics is essentially controlled by the Reynolds

Table 1. Summary of the experimental flow conditions.

occlusion	Re †		v_{max} (cm/s)	v_{min} (cm/s)	D_{max} (cm)	D_{min} (cm)	Re_{max}	Re_{min}	P_{max} (mmHg) ◊	P_{min} (mmHg) ◊
50%	2000	inlet	8.11	0.29	2.49	2.37	1950	100	128	37
		throat	17.7	1.39	1.37	1.12	2290	160	123	35
	1500	inlet	6.13	0.20	2.37	2.28	1422	47	64	24
		throat	12.1	0.49	1.22	1.06	1401	55	59	22
	1100	inlet	4.77	0.20	2.31	2.19	1087	45	43	18
		throat	9.73	0.39	1.13	0.98	1034	43	40	17
35%	2000	inlet	8.39	0.21	2.54	24.03	1983	50	95	18
		throat	12.67	0.51	1.77	1.50	1963	81	92	18
	1500	inlet	7.19	0.32	2.43	2.24	1694	71	45	11
		throat	9.12	0.28	1.64	1.39	1424	43	43	11
	1100	inlet	5.74	0.28	2.35	2.18	1288	65	27	8
		throat	7.58	0.22	1.55	1.31	1107	32	25	8
0%	2000	inlet	7.64	0.49	2.41	2.29	1806	112	133	32

† This value corresponds to the Re number set on the programmable pump. ◊ For P_{max} and P_{min} , the rows "inlet" and "throat" correspond to inlet and outlet of the model respectively.

number (Re), which relates the flow velocity (v) with lumen size (D) as $Re = Dv/\nu$, where ν is the kinematic viscosity of water (1.0×10^{-6} m²/s). Taking into account the internal diameter of our models and the kinematic viscosity of water, the pulsatile pump was programmed to achieve three different peak velocities inside the models: 9.5 cm/s, 7 cm/s and 5 cm/s. This corresponds to peak Reynolds numbers of approximately 2000, 1500 and 1100, respectively, which lie within the physiological range of the aortic artery [42]. Nevertheless, small deviations from these values are expected in the experiments because of the small differences in the mechanical response of the models. Therefore, the exact Reynolds number for each experiment was computed by measuring the internal diameter and the velocity obtained through Echo-PIV. As an example, Figs. 2(c) to 2(e) show the lumen, velocity and Re as a function of time for the $Re = 2000$ experiment in the 50% occluded model. Velocity and diameter are affected by a 5 % error which results in an uncertainty of 10% for Re (grey shadow in Fig. 2(e)). The internal diameter of the model was estimated by tracking the movement of the wall from the B-mode images using an intensity threshold of -6 dB. A summary of the precise experimental conditions is given in Table 1. Repeatability of the experiments, models' mechanical properties and flow patterns was checked from experiments carried out over a five-month period.

In Table 1, the values of "Re" set on the programmable pump and Re_{max} agree within the margins of error for all the experiments. Therefore, in this work we will use the set value to label each experiment. Finally, it is important to mention that the pressure wave-form and the shape of the velocity traces presented in Fig. 1 were preserved for all experiments defining a time reference indicated by the numbered red circles in Fig. 2(d). Times t_1 to t_6 correspond to $0.25T$, $0.40T$, $0.55T$, $0.70T$, $0.85T$ and T , respectively, being T the pulsatile period.

2.5. LCS identification

A common method to identify Lagrangian Coherent Structures (LCS) is by computing the Finite-Time Lyapunov Exponents (FTLE). As demonstrated in [43] the surfaces that

maximize the FTLE field (i.e. ridges) correspond to the LCSs. FTLE measure the rate of separation between initially adjacent particles that are advected by the flow over a finite time interval (τ). Therefore, LCS will represent surfaces of large particle separation, which act as a material barrier identifying regions with different flow dynamics.

To compute the FTLE field the first step consists in seeding the fluid domain with a grid of particles. These particles will be advected from t_0 to $t_0 + \tau$ by integrating the particle velocity field over time. This gives the flow map $\phi_{t_0}^{t_0+\tau} : r(t_0) \rightarrow r(t_0 + \tau)$, where r denotes the particle position. The amount of stretching about a trajectory can be defined in terms of the Cauchy-Green tensor

$$C(r_0, t_0, \tau) = \nabla \phi_{t_0}^{t_0+\tau}(r_0)^\dagger \cdot \nabla \phi_{t_0}^{t_0+\tau}(r_0) \quad (1)$$

evaluated at the initial position $r_0 = r(t_0)$. The maximum stretching $\|\delta r\|_{max}$ ($= \exp^{|\tau|\Lambda} \|\delta r_0\|$) is aligned with the eigenvector of maximum eigenvalue λ_{max} of C . Consequently, the FTLE Λ may be computed as:

$$\Lambda(r_0, t_0, \tau) = \left| \tau^{-1} \right| \ln \sqrt{\lambda_{max}(C(r_0, t_0, \tau))} \quad (2)$$

For unsteady flows, Eq. 2 is computed for a range of times t_0 to provide a time series of the FTLE allowing to follow the dynamics of the LCSs.

Given τ , trajectories can be integrated forward ($\tau > 0$) or backward ($\tau < 0$) in time. For a positive τ , the FTLEs measure the rate of separation, thus identifying repelling structures (Λ^+ field). On the contrary, if τ is negative, the FTLEs measure the rate of convergence, thus identifying attracting structures (Λ^- field). The choice of τ is usually related to the characteristic flow time scales. In this work a characteristic time scale is imposed by the period (T) of the pulsatile flow. Another characteristic time scale is given by the advective time in the post-stenotic region ($D/v \sim 0.3 - 0.5$ s). In light of both time scales, a $\tau = T/3 = 0.35$ s was used in this work.

To obtain sharper fields, FTLEs are usually computed in a grid finer than the original grid used for the particle velocity field. In this work the grid of the particle velocity data was subdivided to contain 3×3 fluid particles. Particles were advected using a 4th order Runge-Kutta method with a cubic interpolation. Further refinement of the particle grid resulted in negligible change in the results. Lastly, as LCSs (i.e. ridges of the FTLE field) we considered all the FTLEs whose value exceeded a threshold of 50% of the maximum value of the FTLE field (this threshold value is larger than the field mean value plus three times its standard deviation).

2.6. Residence time and final position mapping

Particle Residence Time (PRT) maps have shown to be a powerful lagrangian tool when analysing transport phenomena. Each pixel of the map corresponds to the fluid particle's initial position and the pixel value is given by the time spent by this particle within the ROI. To complete the information given by the PRT maps, in this work we introduced the Final Position (FP) maps. Analogous to PRT maps, each pixel of the FP

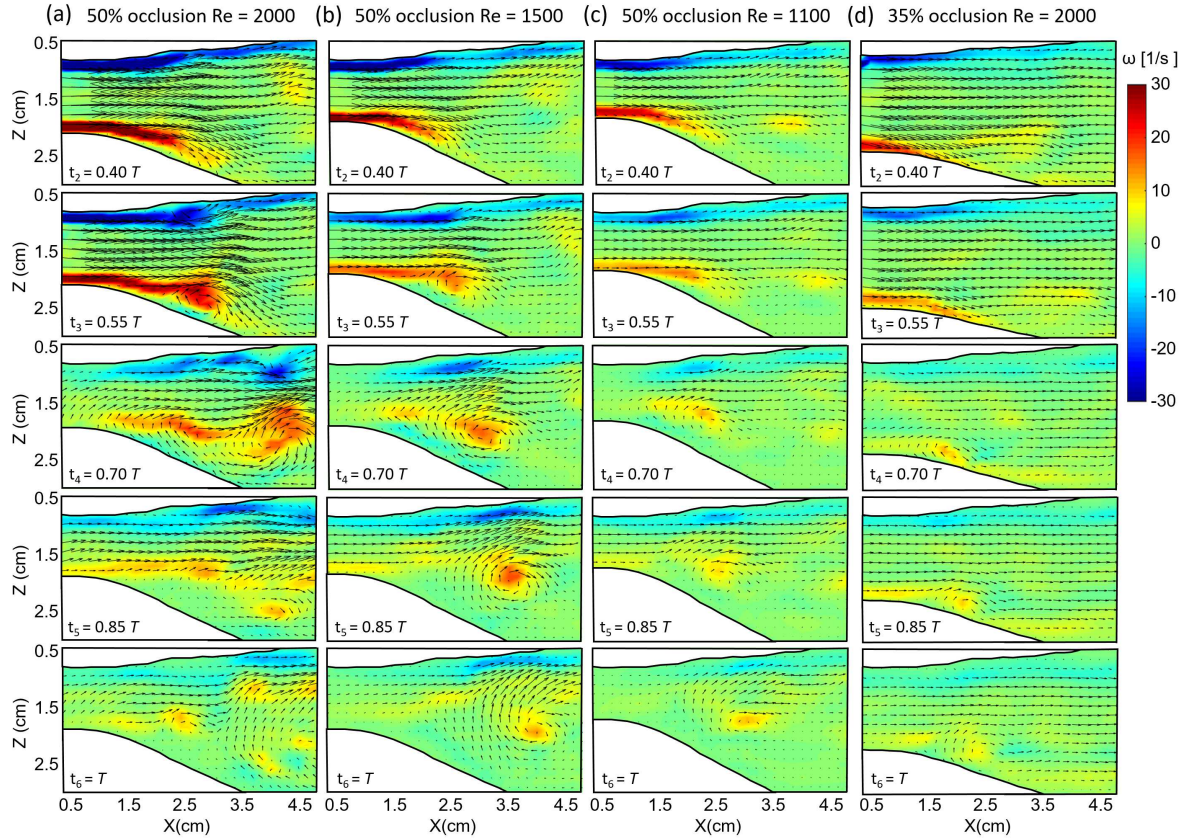


Figure 3. Five snapshots of the instantaneous particle velocity field superimposed over the vorticity field ω for the following experiments (a) 50% occlusion, $Re = 2000$, (b) 50% occlusion, $Re = 1500$, (c) 50% occlusion, $Re = 1100$ and (d) 35% occlusion, $Re = 2000$. Each snapshot corresponds to the times t_2 to t_6 indicated in Fig. 2(d) by the red dots. The color bar is the same for all panels.

map corresponds to the particle's initial position. However, for the FP maps the ROI is subdivided in different color-coded subregions. Then, the pixel value is determined by the fluid particle's final position within these subregions. In this work the post-stenotic ROI was subdivided into three different subregions (please refer to section 3.2.1 for the definition of subregions). For the PRT and FP maps the beginning of the systolic phase ($t = 0$ in Fig. 2(d)) was considered as the initial time. Fluid particles were advected over one pulsatile period following the same procedure described in the preceding subsection.

3. Results

3.1. Eulerian description of the flow: particle velocity and vorticity fields

Flow in the unobstructed model and in the upstream region of the occluded models showed a laminar velocity profile without any flow instabilities (not shown). However, in the post-stenotic region of the occluded models, flow transitioned from laminar to vortex formation and shedding as Re increased. Figure 3 shows five snapshots (times

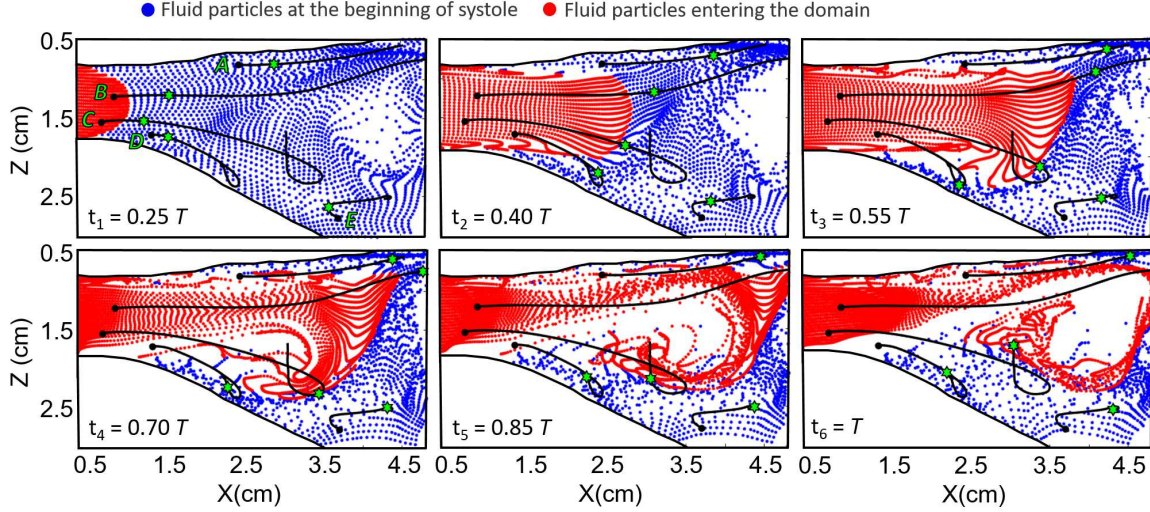


Figure 4. Six snapshots of the particle advection in the 50% occluded model for $Re = 1500$. Particles present at the beginning of the systole ($t = 0$ in Fig 2(d)) are represented in blue dots, while particles entering the domain during one pulsatile period are represented in red. The time reference corresponding to each snapshot is indicated on the left lower corner of each panel. Additionally, in each panel different particle's trajectories (labeled A to E) are represented by black full lines. The full black circle indicates the particle's initial position while the green star represents their position in each snapshot.

t_2 to t_6 in Fig. 2(d)) of the instantaneous velocity field superimposed over the vorticity $\omega = \nabla \times v$ for different experiments. The main features of the flow are highlighted by this figure: a high velocity jet over the stenosis throat and large recirculation region behind the stenosis where vortex form and shed. For a 35% occlusion, at $Re = 2000$ a small recirculation region without shedding appeared behind the stenosis (Fig. 3(d)). Below this Re number flow was mostly laminar. Contrary, for the model with a 50% occlusion, vortex shedding happens for all the Re (Fig. 3 (a)-(c)). As expected, as Re increased the vortices become larger and vorticity values higher. By comparing Figs. 3(a)-(c) vortices not only become larger and stronger but they also propagate faster as Re increased. By tracking the centre of the vortex as a function of time, vortex propagation velocities of 1.9 cm/s, 2.8 cm/s and 6.2 cm/s were found for $Re = 1100$, 1500 and 2000 respectively.

3.2. Lagrangian description of the flow

As shown in Fig. 3 the main structures that govern flow behind the stenosis are the high velocity jet and the vortex. Consequently, those structures will be also responsible for dictating the transport phenomena in the post-stenotic region. Figure 4 shows six snapshots of the fluid particle's advection in the 50% occluded model for $Re = 1500$. Fluid particles at the beginning of the systole (i.e. pre-existing fluid) are represented in blue dots, while fluid particles entering the domain during one pulsatile period are

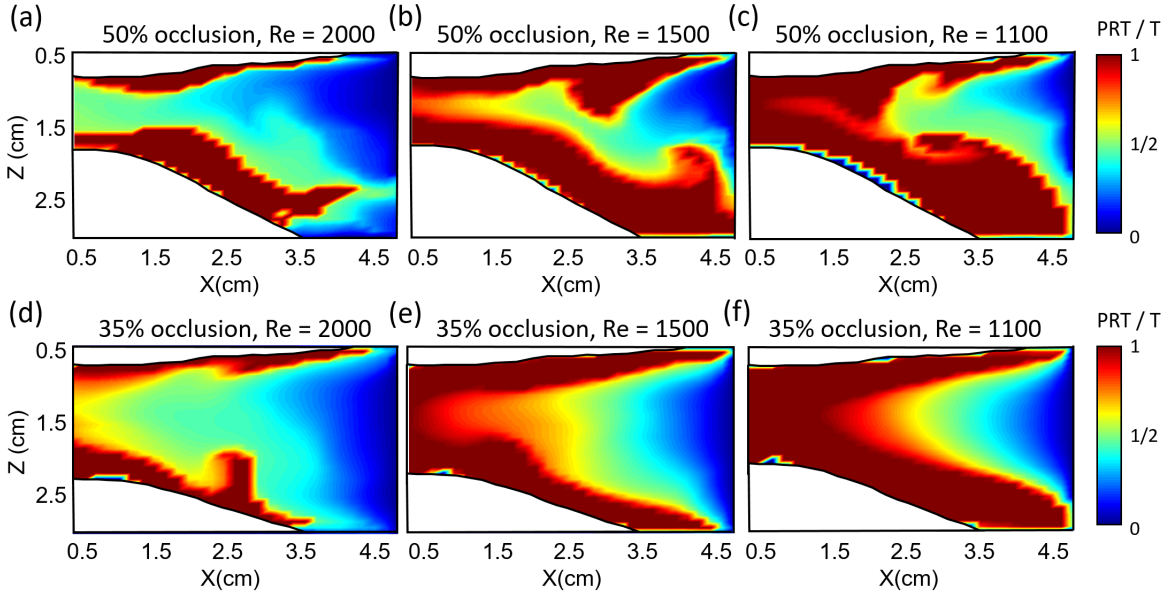


Figure 5. Particle Residence Time (PRT) maps for the following experiments (a) 50% occlusion, $Re = 2000$, (b) 50% occlusion, $Re = 1500$, (c) 50% occlusion, $Re = 1100$, (d) 35% occlusion, $Re = 2000$, (e) 35% occlusion, $Re = 1500$ and (f) 35% occlusion, $Re = 1100$. Each pixel corresponds to the fluid particle’s initial position and the color value to the time spent by the particle within the ROI normalized by the pulsatile period T .

represented in red.

The main features of the fluid transport are highlighted by Fig. 4. As flow enters the domain through the jet, those fluid particles situated at the leading edge of the jet do not mix with the pre-existing fluid. Contrary, mixing occurs mainly in the recirculation zone behind the stenosis where pre-existing fluid is dragged and carried away by the vortex. Finally, there are fluid particles that are relatively stagnant and remain either on or behind the stenosis for the entire cycle. Representative trajectories of these three scenarios are presented in Fig. 4, where the fluid particle’s trajectory and its initial positions are represented by full black lines and a black full circle, respectively. The green star represents the particle’s position for each snapshot. Trajectories *A* and *B* correspond to fluid particles that were pushed downstream by the incoming flow. Trajectory *C* represents a fluid particle that was pushed downstream and then dragged by the vortex. Finally, trajectories *D* and *E* represent stagnant fluid particles on and behind the stenosis, respectively.

3.2.1. Residence time and final position maps To evaluate these different flow behaviours we computed the PRT (Fig. 5) and the FP maps (Fig. 6). For the unobstructed model (not shown) no stagnant regions were observed. All particles travelled across the ROI following an approximately straight path oriented along x-axis. The time for a particle to travel across the ROI was $\approx T$ while the average PRT

over the ROI was $\approx T/2$.

For the occluded models flow behaviour was quite different. Figure 5 shows the PRT maps for the different Re in the occluded models. From Fig. 5 it is possible to identify the two main flow structures: the high velocity jet with low PRT values ($< T/2$) and the recirculation region (on and behind the stenosis) with high PRT values ($> T/2$). For a given Re , the PRT of the fluid particles initially situated in the recirculation region increases with the degree of occlusion. For example, for $Re = 2000$, we observe an overall increase in the PRT by comparing the 50% (Fig. 5(a)) to the 35% (Fig. 5(d)) occluded model. Moreover, we observe that the area occupied by high PRT values (i.e. close to T) is larger for the 50% occluded model. This is consistently observed for the rest of the Re by comparing Figs. 5(b) to 5(e) and Figs. 5(c) to 5(f). Lastly, for a given degree of occlusion (Figs. 5(a) to 5(c) for a 50% occlusion and Figs. 5(d) to 5(f) for a 35% occlusion), the PRT over the ROI increases as Re decreases.

Since Fig. 5 only gives us information about the time a fluid particle spent within the ROI without any information on its position, we complete this temporal information by introducing the FP maps (Fig. 6). For the FP maps the ROI was subdivided into three different subregions representing: (i) the region occupied by the jet, (ii) the region on the stenosis and (iii) the region behind the stenosis. Those regions are indicated by white dashed lines in Fig. 6. More precisely, region i goes from the anterior wall of the model (i.e. proximal to the ultrasonic array) to the stenosis throat, occupying the whole post-stenotic region along the x-direction. Regions ii and iii both go from the stenosis throat to the posterior wall. However, region ii goes from $X \approx 0.4$ cm to $X \approx 3$ cm, while region iii goes from $X \approx 3$ cm to $X \approx 4.8$ cm, representing the regions on and behind the stenosis, respectively. The choice of these regions allowed us to evaluate the three different scenarios described above for Fig. 4: fluid particles pushed by the flow, fluid particles dragged by the vortex and stagnant particles that stayed on and behind the stenosis. In Fig. 6 the colours cyan, orange and red correspond to a fluid particle's final position within regions i , ii and iii , respectively, while the color blue is for particles that have left the region.

In Fig. 6, we observe that part of the fluid particles with high PRT values, which initially were located on the stenosis (region ii), moved to region iii while the rest remained on the stenosis (i.e. region ii). The number of particles remaining on the stenosis does not strongly depend on Re . By comparing Figs. 6(a) to 6(c) and Figs. 6(d) to 6(f) we observe that the size of the orange surface remains approximately the same. However, we observe that the lower the Re the more particles remain in region i and iii . Finally, we also observe some cyan regions within region ii for Figs. 6(a) and 6(b). These regions correspond to fluid particles that were dragged into region i by the vortex.

3.2.2. FTLE fields Figure 7 shows six snapshots of the instantaneous ridges of the FTLE fields superimposed to the instantaneous velocity field for different experiments. Each snapshot corresponds to the time reference set in Fig. 2(d). Blue and red ridges

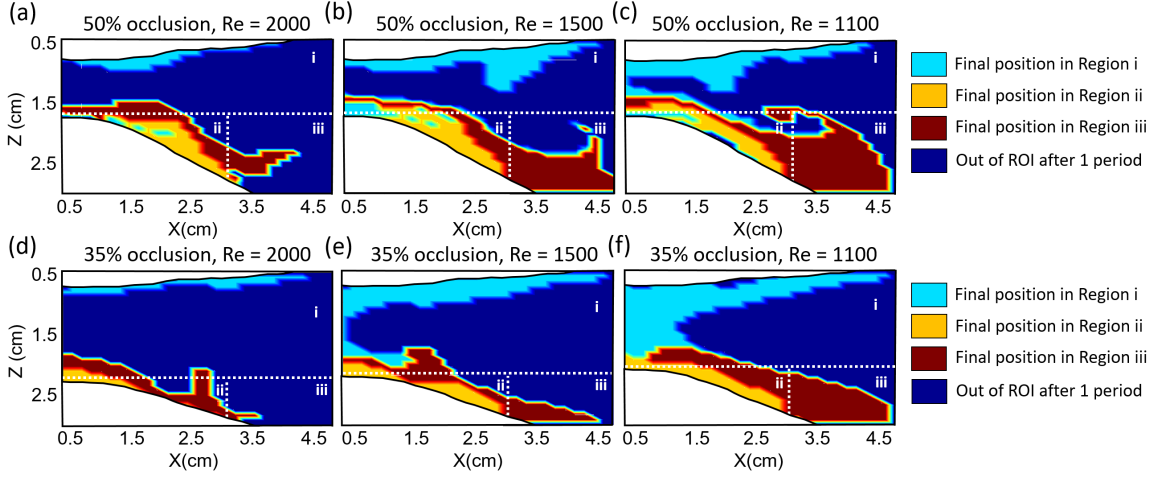


Figure 6. Final Position (FP) maps for the following experiments: (a) 50% occlusion, $Re = 2000$, (b) 50% occlusion, $Re = 1500$, (c) 50% occlusion, $Re = 1100$, (d) 35% occlusion, $Re = 2000$, (e) 35% occlusion, $Re = 1500$ and (f) 35% occlusion, $Re = 1100$. Each pixel corresponds to the fluid particle’s initial position and the color value corresponds to the particle’s final position within a given subregion: colours cyan, orange and red correspond to subregion *i*, *ii* and *iii*, respectively, which are indicated by a dashed white line. The color blue is for particles that left the region in one period.

corresponds to the attracting (Λ^+) and repelling (Λ^-) LCSs respectively. We observed several LCSs related to the high velocity jet and the vortex. The LCS indicated by *I* is related to the leading edge of the central jet. This attracting LCS separates the incoming flow from the pre-existing fluid. We observe that the intensity and the extension of this barrier increases with Re . Moreover, the LCSs denoted by *IIa* and *IIb* in Fig. 7 are related to the vortex. Both LCSs surround the vortex at all times and are the main responsible for the mixing behind the stenosis. Fluid particles trapped between those barriers travel along the vortex, repelled by LCS *IIa* (red) and simultaneously attracted by LCS *IIb* (blue). Moreover, we observe that the strength of both barriers increase with Re while the overall structure is maintained. Finally, an additional vortex on the anterior wall of the model is observable in Figs. 7(a) and 7(b). This vortex is more evident from the FTLE fields than from the vorticity field presented in Figs 3(a) and 3(b).

4. Discussion

In this work a novel approach which combines ultrasound with Eulerian and Lagrangian descriptors has been applied to study vortex dynamics and transport phenomena in stenotic aortic models with morphology, mechanical and optical properties close to those of real arteries. We observed that the flow in the post-stenotic region is composed of two main structures: a high velocity jet over the stenosis throat and a recirculation region behind the stenosis where vortex form and shed. This result is consistent with

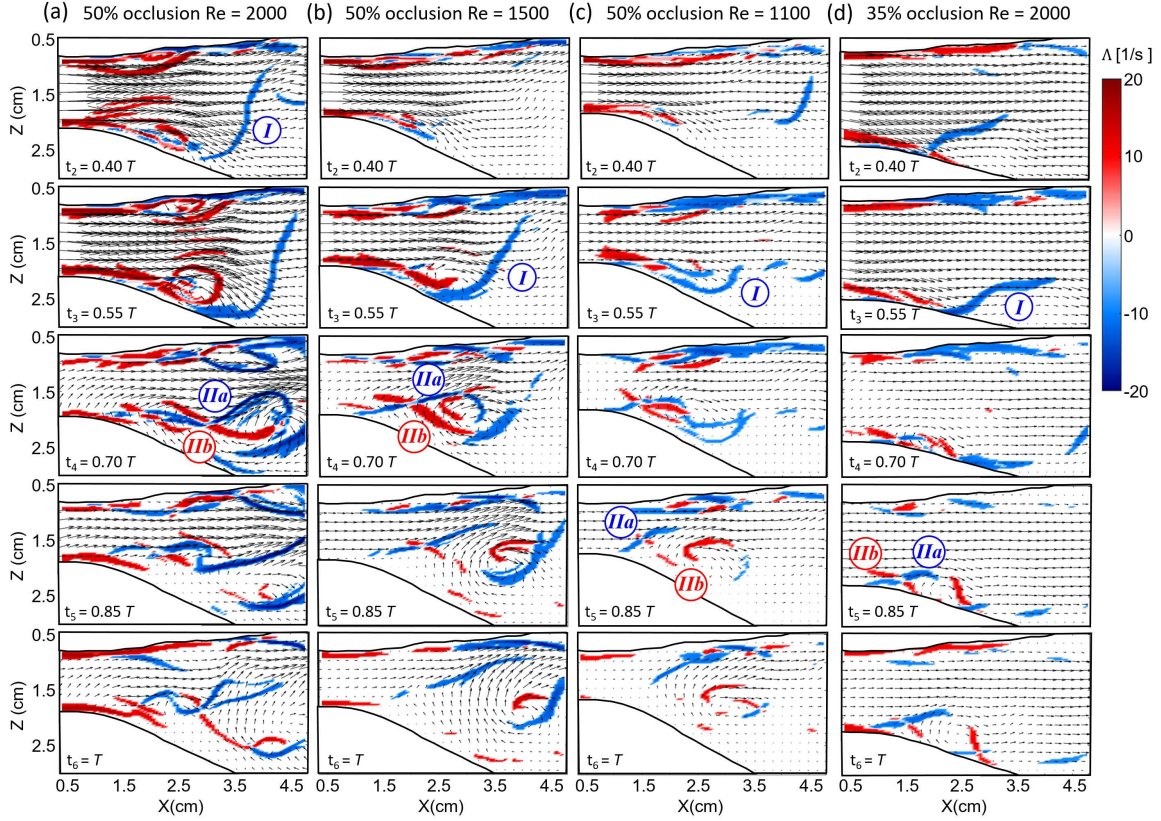


Figure 7. Six snapshots of the instantaneous ridges of the FTLE fields superimposed to the instantaneous particle velocity field for the following experiments (a) 50% occlusion, $Re = 2000$, (b) 50% occlusion, $Re = 1500$, (c) 50% occlusion, $Re = 1100$ and (d) 35% occlusion, $Re = 2000$. Each snapshot corresponds to the times t_2 to t_6 indicated in Fig. 2(d). Attracting (Λ^+) and repelling (Λ^-) LCSs are represented in blue and red respectively. The color-scale is the same for all panels.

previous numerical and experimental studies conducted in axis-symmetric [7, 10, 11] and non-symmetrical models [12, 9].

For those experiments where vortex shedding was observed, we were able to track the vortex center from the vorticity snapshots and measure its axial velocity of propagation. Although we could not find any values reported in the literature for the vortex velocity of propagation in stenotic vessels, we were able to deduce them from the work of Geoghegan *et al.* [10]. The values obtained in our work are smaller by factor ~ 10 when compared to the results deduced from [10]. However, those experiments were conducted in an axis-symmetrically occluded silicone model. Since the Re used in our experiments and in [10] are similar, the difference between the results is probably related to the elasticity difference between models, since silicone is far less compliant than PVA. Moreover, in their work they report a Kelvin-Helmholtz instability, which we do not observe in our experiments due to the asymmetry of our model. This is consistent with [9, 12].

By computing the FTLE fields (Fig. 7), we were able to identify different material

barriers associated to the vortex and the leading edge of the jet. Analogous LCSs were reported by previous studies but in significantly different hemodynamic situations. For example, in [23] and [19] FTLE fields were computed to study transport in the left ventricle. In those studies, they found that during the left ventricle filing the backward FTLE field reveals a well-defined LCS that separates the injected blood from the pre-existing one. Other numerical studies in abdominal aortic aneurysm showed analogous behavior during diastole [13, 31]. The LCS described in these works is analogous to the attracting barrier I identified in Fig. 7. However, contrary to what is described in [19, 23, 13, 31], due to the asymmetric nature of our models and flow, the LCS I does not roll originating a vortex ring whose trailing edge (i.e. facing upstream) is enclosed by a repelling barrier. This is evident from Fig. 7(a) for times t_5 and t_6 : as vortex leave the post-stenotic region there are still ridges of the FTLE field separating the jet from the recirculation region.

In this work we also identified material barriers associated to the vortex (LCSs IIa and IIb in Fig. 7). Both LCSs surround the vortex at all times and are the main responsible for the mixing between the incoming and the pre-existing fluid as described in [44]. By comparing Figs. 4 and 7(b) we observed that during vortex build up, pre-existing fluid gets trapped between barriers IIa and IIb and travel along the vortex getting mixed and stirred with the incoming flow. Similar dynamics were also observed for $Re = 2000$ and 1100 , although it was not illustrated in Fig. 4. For the 35% occluded model at $Re = 2000$ those barriers were also visible around the vortex (specially for times t_5 and t_6 in Fig. 7(d)). Analogous results were reported by computing the FTLE fields from numerical studies in aortic aneurysm [31, 13] and in the experimental work of Vetel *et al.* in a rigid model of a carotid bifurcation [30]. Lastly, in this work we showed that the strenght of this barriers increases with Re and consequently with vorticity.

To complete the information conveyed by the FTLE fields we computed the PRT and the FP maps. Particularly, PRT and FP maps as defined in this work, provide detailed information on the transport of the pre-existing fluid (blue dots in Fig. 4). By comparing Figs. 5 and 6, we observed that part of the fluid initially located on the stenosis (region *ii*), moved to region *iii* while the rest remained stagnant on the stenosis. In Fig. 6 we observed that the number of these stagnant particles does not strongly depend on Re for the range of values explored in this work. Contrary, results reported by Jerónimo *et al.* indicate that the number of stagnant particles increases as Re increases [29], however, comparison between their results and the ones reported in this work is not straightforward. In [29] they used peak Re ranging from 7200 to 28080 in a rigid smooth axisymmetric constriction followed by an unrealistic sudden expansion, which is quite different from the setup used in this work.

As in [29], our experiments were also limited by the acquisition time of the ultrasound scanner and the velocity imaging through Echo-PIV was restricted to the centre plane of the model. The current setup did not allow the study of the three dimensional nature of the flow. Future studies should aimed in incorporating three dimensional information on vortical structures and transport phenomena. This can be

implemented with the advent of new 3D ultrasound imaging technologies [45] like matrix [46] and row-columns [47] arrays.

Lastly, LCS, PRT and FP maps may provide an alternative approach to understand stenosis growth. As shown by [14] platelet activation potential is maximized along the LCSs. Moreover, from the PRT and FP maps we showed that stagnant particles remained on stenosis after one pulsatile period. These stagnant particles spend more time on the stenosis where platelet activation potential is large (i.e. large FTLE values as in Fig. 7) which may favour blood clot formation leading to stenosis growth.

5. Conclusion

By using a novel approach which combines ultrasound with Eulerian and Lagrangian descriptors, we analysed the flow dynamics and transport phenomena in stenotic aortic models with morphology, mechanical and optical properties close to those of real arteries. To this end, vorticity, FTLEs, PRT and FP maps were computed from the particle velocity fields acquired using Echo-PIV. We characterized vortex kinematics showing that vortex propagation velocity increases with Re number. From the FTLE field we identified material barriers that dictate transport behind the stenosis. The size and strength of these barrier is also Re depend. Lastly, from the PRT and FP maps, we showed that even for the highest Re , fluid parcels remain on the stenosis which combined with large FTLE values may provide an alternative way to understand the process of stenosis growth. This comprehensive study proves that this type of approach may help to bridge the gap between fundamental physics and relevant clinical applications such as plaque evolution and rupture.

Acknowledgments

This work was supported by CSIC I+D 2016 Project “Estudio de la dinamica de un flujo pulsatil y sus implicancias en hemodinamica vascular” Uruguay, ANII-Uruguay, PEDECIBA Física - Uruguay, the Administrative Department of Science, Technology and Innovation of the Colombian Government (Colciencias) and the Research and Development Center (CIDI) of the Universidad Pontificia Bolivariana through the program “Es tiempo de Volver” (Grant number 548B-01/16-04), Colombia. Nicasio Barrere acknowledges a doctoral scholarship (POSNAC-2015-1-109843) from ANII-Uruguay.

References

- [1] S. Mendis, P. Puska, B. Norrving, W. H. Organization, *et al.*, *Global atlas on cardiovascular disease prevention and control*. World Health Organization, 2011.
- [2] J. Bermejo, Y. Benito, M. Alhama, R. Yotti, P. Martínez-Legazpi, C. P. Del Villar, E. Pérez-David, A. González-Mansilla, C. Santa-Marta, A. Barrio, *et al.*, “Intraventricular vortex properties in

- nonischemic dilated cardiomyopathy,” *American Journal of Physiology-Heart and Circulatory Physiology*, vol. 306, no. 5, pp. H718–H729, 2014.
- [3] G.-R. Hong, G. Pedrizzetti, G. Tonti, P. Li, Z. Wei, J. K. Kim, A. Baweja, S. Liu, N. Chung, H. Houle, *et al.*, “Characterization and quantification of vortex flow in the human left ventricle by contrast echocardiography using vector particle image velocimetry,” *JACC: Cardiovascular Imaging*, vol. 1, no. 6, pp. 705–717, 2008.
- [4] R. Faludi, M. Szulik, J. D’hooge, P. Herijgers, F. Rademakers, G. Pedrizzetti, and J.-U. Voigt, “Left ventricular flow patterns in healthy subjects and patients with prosthetic mitral valves: an in vivo study using echocardiographic particle image velocimetry,” *The Journal of thoracic and cardiovascular surgery*, vol. 139, no. 6, pp. 1501–1510, 2010.
- [5] C. K. Zarins, D. P. Giddens, B. Bharadvaj, V. S. Sottiurai, R. F. Mabon, and S. Glagov, “Carotid bifurcation atherosclerosis. quantitative correlation of plaque localization with flow velocity profiles and wall shear stress.,” *Circulation research*, vol. 53, no. 4, pp. 502–514, 1983.
- [6] J. Martorell, P. Santoma, K. Kolandaivelu, V. B. Kolachalama, P. Melgar-Lesmes, J. J. Molins, L. Garcia, E. R. Edelman, and M. Balcells, “Extent of flow recirculation governs expression of atherosclerotic and thrombotic biomarkers in arterial bifurcations,” *Cardiovascular research*, vol. 103, no. 1, pp. 37–46, 2014.
- [7] S. S. Varghese, S. H. Frankel, P. F. Fischer, *et al.*, “Direct numerical simulation of stenotic flows. part 2. pulsatile flow,” *Journal of Fluid Mechanics*, vol. 582, no. 1, pp. 281–318, 2007.
- [8] D. Katritsis, A. Theodorakakos, I. Pantos, A. Andriotis, E. Efstathopoulos, G. Siontis, N. Karcanias, S. Redwood, and M. Gavaises, “Vortex formation and recirculation zones in left anterior descending artery stenoses: computational fluid dynamics analysis,” *Physics in Medicine & Biology*, vol. 55, no. 5, p. 1395, 2010.
- [9] W. Choi, J. H. Park, H. Byeon, and S. J. Lee, “Flow characteristics around a deformable stenosis under pulsatile flow condition,” *Physics of Fluids*, vol. 30, no. 1, p. 011902, 2018.
- [10] P. Geoghegan, N. Buchmann, J. Soria, and M. C. Jermy, “Time-resolved piv measurements of the flow field in a stenosed, compliant arterial model,” *Experiments in fluids*, vol. 54, no. 5, p. 1528, 2013.
- [11] K. Pielhop, M. Klaas, and W. Schröder, “Analysis of the unsteady flow in an elastic stenotic vessel,” *European Journal of Mechanics-B/Fluids*, vol. 35, pp. 102–110, 2012.
- [12] A. Y. Usmani and K. Muralidhar, “Pulsatile flow in a compliant stenosed asymmetric model,” *Experiments in Fluids*, vol. 57, no. 12, p. 186, 2016.
- [13] S. C. Shadden and C. A. Taylor, “Characterization of coherent structures in the cardiovascular system,” *Annals of biomedical engineering*, vol. 36, no. 7, pp. 1152–1162, 2008.
- [14] S. C. Shadden and S. Hendabadi, “Potential fluid mechanic pathways of platelet activation,” *Biomechanics and modeling in mechanobiology*, vol. 12, no. 3, pp. 467–474, 2013.
- [15] Z. Xu, N. Chen, S. C. Shadden, J. E. Marsden, M. M. Kamocka, E. D. Rosen, and M. Alber, “Study of blood flow impact on growth of thrombi using a multiscale model,” *Soft Matter*, vol. 5, no. 4, pp. 769–779, 2009.
- [16] V. Rayz, L. Bousset, L. Ge, J. Leach, A. Martin, M. Lawton, C. McCulloch, and D. Saloner, “Flow residence time and regions of intraluminal thrombus deposition in intracranial aneurysms,” *Annals of biomedical engineering*, vol. 38, no. 10, pp. 3058–3069, 2010.
- [17] G. Haller, “Lagrangian coherent structures,” *Annual Review of Fluid Mechanics*, vol. 47, pp. 137–162, 2015.
- [18] S. C. Shadden, *Lagrangian Coherent Structures*. Wiley Online Library, 2012.
- [19] S. Espa, M. G. Badas, S. Fortini, G. Querzoli, and A. Cenedese, “A lagrangian investigation of the flow inside the left ventricle,” *European Journal of Mechanics-B/Fluids*, vol. 35, pp. 9–19, 2012.
- [20] L. Rossini, P. Martinez-Legazpi, V. Vu, L. Fernandez-Friera, C. P. del Villar, S. Rodriguez-Lopez, Y. Benito, M.-G. Borja, D. Pastor-Escuredo, R. Yotti, *et al.*, “A clinical method for mapping and quantifying blood stasis in the left ventricle,” *Journal of biomechanics*, vol. 49, no. 11,

- pp. 2152–2161, 2016.
- [21] M. G. Badas, F. Domenichini, and G. Querzoli, “Quantification of the blood mixing in the left ventricle using finite time lyapunov exponents,” *Meccanica*, vol. 52, no. 3, pp. 529–544, 2017.
 - [22] G. Di Labbio, J. Vétel, and L. Kadem, “Material transport in the left ventricle with aortic valve regurgitation,” *Physical Review Fluids*, vol. 3, no. 11, p. 113101, 2018.
 - [23] S. Hendabadi, J. Bermejo, Y. Benito, R. Yotti, F. Fernández-Avilés, J. C. Del Álamo, and S. C. Shadden, “Topology of blood transport in the human left ventricle by novel processing of doppler echocardiography,” *Annals of biomedical engineering*, vol. 41, no. 12, pp. 2603–2616, 2013.
 - [24] J. Töger, M. Kanski, M. Carlsson, S. J. Kovács, G. Söderlind, H. Arheden, and E. Heiberg, “Vortex ring formation in the left ventricle of the heart: analysis by 4d flow mri and lagrangian coherent structures,” *Annals of biomedical engineering*, vol. 40, no. 12, pp. 2652–2662, 2012.
 - [25] J. J. Charonko, R. Kumar, K. Stewart, W. C. Little, and P. P. Vlachos, “Vortices formed on the mitral valve tips aid normal left ventricular filling,” *Annals of biomedical engineering*, vol. 41, no. 5, pp. 1049–1061, 2013.
 - [26] M. H. Babiker, L. F. Gonzalez, F. Albuquerque, D. Collins, A. Elvikis, C. Zwart, B. Roszelle, and D. H. Frakes, “An in vitro study of pulsatile fluid dynamics in intracranial aneurysm models treated with embolic coils and flow diverters,” *IEEE Transactions on Biomedical Engineering*, vol. 60, no. 4, pp. 1150–1159, 2012.
 - [27] S. Patel, A. Y. Usmani, and K. Muralidhar, “Effect of aorto-iliac bifurcation and iliac stenosis on flow dynamics in an abdominal aortic aneurysm,” *Fluid Dynamics Research*, vol. 49, no. 3, p. 035513, 2017.
 - [28] M. D. Jeronimo, K. Zhang, and D. E. Rival, “Direct lagrangian measurements of particle residence time,” *Experiments in Fluids*, vol. 60, no. 4, p. 72, 2019.
 - [29] M. Jeronimo and D. Rival, “Particle residence time in pulsatile post-stenotic flow,” *Physics of Fluids*, vol. 32, no. 4, p. 045110, 2020.
 - [30] J. Vétel, A. Garon, and D. Pelletier, “Lagrangian coherent structures in the human carotid artery bifurcation,” *Experiments in fluids*, vol. 46, no. 6, pp. 1067–1079, 2009.
 - [31] A. Arzani and S. C. Shadden, “Characterization of the transport topology in patient-specific abdominal aortic aneurysm models,” *Physics of Fluids*, vol. 24, no. 8, p. 081901, 2012.
 - [32] M. Bernal, J. Saldarriaga, C. Cabeza, C. Negreira, J. Bustamante, and J. Brum, “Development and evaluation of anisotropic and nonlinear aortic models made from clinical images for in vitro experimentation,” *Physics in Medicine & Biology*, vol. 64, no. 16, p. 165006, 2019.
 - [33] M. Bernal, I. Sen, and M. W. Urban, “Evaluation of materials used for vascular anastomoses using shear wave elastography,” *Physics in Medicine & Biology*, vol. 64, no. 7, p. 075001, 2019.
 - [34] D. S. Bagnasco, F. M. Ballarin, L. J. Cymberknop, G. Balay, C. Negreira, G. A. Abraham, and R. L. Armentano, “Elasticity assessment of electrospun nanofibrous vascular grafts: A comparison with femoral ovine arteries,” *Materials Science and Engineering: C*, vol. 45, pp. 446–454, 2014.
 - [35] G. Balay, J. Brum, D. Bia, R. Armentano, and C. Negreira, “Improvement of artery radii determination with single ultra sound channel hardware & in vitro artificial heart system,” in *2010 Annual International Conference of the IEEE Engineering in Medicine and Biology*, pp. 2521–2524, IEEE, 2010.
 - [36] H.-B. Kim, J. R. Hertzberg, and R. Shandas, “Development and validation of echo piv,” *Experiments in fluids*, vol. 36, no. 3, pp. 455–462, 2004.
 - [37] H. Zheng, L. Liu, L. Williams, J. R. Hertzberg, C. Lanning, and R. Shandas, “Real time multicomponent echo particle image velocimetry technique for opaque flow imaging,” *Applied physics letters*, vol. 88, no. 26, p. 261915, 2006.
 - [38] J. A. Jensen, S. I. Nikolov, C. Alfred, and D. Garcia, “Ultrasound vector flow imaging—part i: Sequential systems,” *IEEE transactions on ultrasonics, ferroelectrics, and frequency control*, vol. 63, no. 11, pp. 1704–1721, 2016.
 - [39] G. Montaldo, M. Tanter, J. Bercoff, N. Benech, and M. Fink, “Coherent plane-wave compounding for very high frame rate ultrasonography and transient elastography,” *IEEE transactions on*

- ultrasonics, ferroelectrics, and frequency control*, vol. 56, no. 3, pp. 489–506, 2009.
- [40] W. Thielicke and E. Stamhuis, “Pivlab—towards user-friendly, affordable and accurate digital particle image velocimetry in matlab,” *Journal of open research software*, vol. 2, no. 1, 2014.
- [41] M. F. O’Rourke, J. V. Blazek, C. L. Morreels Jr, and L. J. Krovetz, “Pressure wave transmission along the human aorta: changes with age and in arterial degenerative disease,” *Circulation Research*, vol. 23, no. 4, pp. 567–579, 1968.
- [42] H. Ha, M. Ziegler, M. Welander, N. Bjarnegård, C.-J. Carlhäll, M. Lindenberg, T. Länne, T. Ebbens, and P. Dyverfeldt, “Age-related vascular changes affect turbulence in aortic blood flow,” *Frontiers in physiology*, vol. 9, p. 36, 2018.
- [43] S. C. Shadden, F. Lekien, and J. E. Marsden, “Definition and properties of lagrangian coherent structures from finite-time lyapunov exponents in two-dimensional aperiodic flows,” *Physica D: Nonlinear Phenomena*, vol. 212, no. 3-4, pp. 271–304, 2005.
- [44] S. C. Shadden, K. Katija, M. Rosenfeld, J. E. Marsden, and J. O. Dabiri, “Transport and stirring induced by vortex formation,” *Journal of Fluid Mechanics*, vol. 593, p. 315, 2007.
- [45] J. A. Jensen, S. I. Nikolov, C. Alfred, and D. Garcia, “Ultrasound vector flow imaging—part ii: Parallel systems,” *IEEE transactions on ultrasonics, ferroelectrics, and frequency control*, vol. 63, no. 11, pp. 1722–1732, 2016.
- [46] M. Correia, J. Provost, M. Tanter, and M. Pernot, “4d ultrafast ultrasound flow imaging: in vivo quantification of arterial volumetric flow rate in a single heartbeat,” *Physics in Medicine & Biology*, vol. 61, no. 23, p. L48, 2016.
- [47] J. Sauvage, M. Flesch, G. Férin, A. Nguyen-Dinh, J. Porée, M. Tanter, M. Pernot, and T. Deffieux, “A large aperture row column addressed probe for in vivo 4d ultrafast doppler ultrasound imaging,” *Physics in Medicine & Biology*, vol. 63, no. 21, p. 215012, 2018.